ADVANCED FUNCTIONAL MATERIALS
www.afm-journal.de

Active-Textile Yarns and Embroidery Enabled by Wet-Spun Liquid Crystalline Elastomer Filaments

*Antonio Proctor Martinez, Alicia Ng, So Hee Nah, and Shu Yang**

Liquid crystal elastomers (LCEs) are promising candidates for creating adaptive textile-based devices that can actively and reversibly respond to the environment for sensing and communication. Despite recent advances in scalable manufacturing of LCE filaments for textile engineering, the actuation modes of various LCE filaments focus on contractual deformations. In this study, manufacture of polydomain LCE filaments with potential scalability by wet-spinning is studied, followed by mechanical exploitation to program liquid crystal mesogen alignments, demonstrating both contractual and twisting actuation profiles. By plying these LCE filaments into yarns with different twist concentrations, yarn actuation, and mechanical performance is tuned. Yarns plied at 4 twists per cm can generate up to a seven-fold increase in elastic modulus while maintaining 90% of actuation strain performance from their native filament. The contractual and twisting LCE filaments are then embroidered with varying stitch types to spatially program complex 2D-to-3D transformations in "inactive" fabrics. It is shown that a running stitch can actuate up to 15% in strain and create angular displacements in fabric with twisted mesogen alignments. It is envisioned that the wet-spun polydomain LCE filaments for diverse plied yarn production together with textile engineering will open new opportunities to design smart textiles and soft robotics.

1. Introduction

Textiles, which encompass hierarchical networks of inter-lacing or inter-looping fibers, filaments, or yarns, are known for their flexibility, conformability, and breathability.[1] They offer a unique opportunity for programming material properties at various length scales.[1] However, to create textile-based devices that can actively respond to environments for sensing and communication, it requires bringing material intelligence into the fibers and filaments that compose the higher-order textiles such as yarns and fabrics.[1–4] Liquid crystal elastomers (LCEs), highly regarded for their reversible shape memory, are such intelligent materials.[5] LCEs are lightly-cross-linked polymer networks containing liquid crystal (LC) mesogens along the polymer backbone or in the side chains, and are capable of adapting their shape, size, and/or color in response to external stimuli (e.g., heat,[2–4,6–11] electric fields,[12] magnetic fields,[13] and/or light[14–16]).[5] The intrinsic anisotropy of the mesogens with an elastomeric network allows for fast and reversible anisotropic deformations (up to 500% strain[17] and as fast as 10 ms[18]) when heated above the nematic-to-isotropic phase transition temperature (T_{NI}). Therefore, the production of LCE fibers and filaments is emerging for potential applications in soft robotics[7–11] and smart textiles,[2–4] where anisotropy can amplify application performance (e.g., work capacity[7,9] or fabric breathability[4]), while attaining the structural components of conventional textiles that provide compliance and fit to the wearer or system.

So far, the production of LCE filaments relies on processes derived from additive manufacturing, including direct ink writing,[2,7] melt drawing,[8–11,19–21] or melt electrowriting,[22] where LC mesogen alignment within the filaments is directed by the shear flow,[2,7–11,19–22] followed by immediate UV cross-linking upon extrusion to lock the alignment. These processes, rapid and scalable, have been combined with textile engineering[1,18] to create higher-order textile-based structures, e.g. woven[3] and knitted fabrics,[4] braids.[23] However, the deformation profile of the fabricated LCE filaments is mainly contractual. LCE fibers with bending[24–26] and twisting[26–29] profiles have been fabricated using a mold, where the alignment of LC mesogens is either directed by the surface chemistry of the mold,[26] or by stretching or twisting the casted polydomain filaments.[27–29] Nevertheless, these fibers or filaments are fabricated at the centimeter scale, falling short of scaling up the textile hierarchy. It will be highly desirable to develop a scalable process that can expand mesogen programming for more dynamic and diverse deformation profiles at meter scales.

A. P. Martinez, A. Ng, S. H. Nah, S. Yang
Department of Materials Science and Engineering
University of Pennsylvania
3231 Walnut Street, Philadelphia, PA 19104, USA
E-mail: shuyang@seas.upenn.edu

The ORCID identification number(s) for the author(s) of this article can be found under https://doi.org/10.1002/adfm.202400742

DOI: 10.1002/adfm.202400742

Here, we present a continuous wet-spinning method as a step towards the scalable manufacture of polydomain LCE filaments, followed by the mechanical induction of mesogen alignments to achieve bi-modal actuation profiles (contractual and twisting) in meter-long LCE filaments. With filaments of different profiles, we explore filament assembly (yarn plying) and textile structuring (embroidery) techniques to modulate mechanical and actuation performance. We confirm that actuation profiles of the native filaments are maintained in the yarns and show that an increased twist concentration (4 twists per cm) can generate up to a sevenfold increase in elastic modulus. Next, we embroider the LCE filaments to explore the relationship between mesogen alignment and stitch type. We find that a running stitch outperforms a backstitch in an inactive cotton fabric, maintaining ≈50% of the LCE filament's contraction-based actuation performance and translating the rotation-based actuation into an angular displacement in the inert fabric.

2. Results and Discussion

2.1. Fabrication of Wet-Spun Liquid Crystal Elastomer (LCE) Filaments

Manufacture of the filaments in the polydomain state notably provides freedom for mesogen alignment through mechanical deformation (in contrast to those automatically manufacturing in the monodomain state) and thus, increased opportunity for diverse actuation profiles. To manufacture a polydomain filament, we leveraged a wet-spinning methodology, known as reaction spinning.[30] While polydomain filaments could be manufactured through additive-manufacturing-based methods at a decreased extrusion pressure or extrusion rate, the filaments often have flattened or non-uniform morphologies due to the need for a printing substrate.[2,6,7,21] Similarly, the dimension of the LCE filaments may experience non-uniform shrinkage due to the confinement of the substrate. While a few approaches have been attempted to address these issues,[2,6,7,15,20,21] very few have resolved all issues, including rapid solidification, cylindrical morphologies, uniform shrinkage, and scalability in producing meter-scale polydomain LCE filaments.[19]

Here, we have formulated an LCE precursor spinning ink that would undergo thiol-Michael addition reactions, which are notably insensitive to oxygen or water[31] in the coagulation bath (see **Figure 1**a for reagents; Figure S1, Supporting Information for the related reactions, Movie S1, Supporting Information for ink fabrication). The precursor spinning ink was composed of mesogen (1,4-bis-[4-(3-acryloyloxypropyloxy)benzoyloxy]−2-methylbenzene (RM257), with thiol-based chain extender 2,2-(ethylenedioxy) diethanethiol (EDDT) and cross-linker pentaerythritol tetrakis(3-mercaptopropionate) (PETMP), dissolved in a nematic solvent, 4-cyano-4′-pentylbiphenyl (5CB). 5CB not only helped to modulate the ink viscosity to facilitate extrusion but also helped to maintain the nematic ordering despite the inclusion of the thiol-based reagents (Figure S2, Supporting Information), which are intrinsically isotropic. It should be noted that the catalyst used to initiate the thiol-Michael addition reactions, dipropylamine (DPA), was present in the coagulation bath composed of a nonsolvent, deionized (DI) water, instead of the spinning ink. Figure 1b illustrates the wet-spinning process used to coagulate the filaments. The success of the reaction spinning process relied on the rapid polymerization of RM257 with EDDT and crosslinking with PETMP (catalyzed by the exposure to and diffusion of DPA, see Movie S1, Supporting Information for real-time coagulation of spinning ink). Separating the catalyst and reagent materials was critical; it increased the stability of the precursor spinning ink, which would otherwise react with each other within minutes and significantly increase the ink viscosity, making it difficult to extrude uniform filaments. Similarly, the use of a nonsolvent, deionized (DI) water, for the coagulation bath helped to keep the spinning ink from dispersing into the bath. To rapidly coagulate the ink in the bath, we overloaded the amount of catalyst (DPA) to saturation in DI water (3.5 wt.%). As a proof-of-concept to showcase the potential scalability of the wet spinning method reported here, we manufactured a 12m long LCE filament (see filament at 24 h after spinning in Figure 1c). Since wet spinning is a continuous manufacturing method, in theory, the filament can be generated at any length so long that there is enough ink, and the syringe pump and winding roller remain stable over a long period of time. The coagulating bath (Figure S3, Supporting Information) is designed to provide full immersion of the filament in DPA/DI water for ≈45 s at an ink flow rate of 100 μL min^{-1}. The diffusion of DPA into the filament extruded from an 18-gauge needle allowed the thiol-Michael addition reactions to complete at 12 min post-collection, which was confirmed by Fourier-transform infrared (FT-IR) spectra (Figure S4, Supporting Information). Scanning electron microscopy (SEM) images showed that the cross sections of the wet-spun LCE filaments extruded from a 3 mL syringe were cylindrical, with an average diameter of 769.8 ± 2.73 μm (Figure 1d), smaller than the inner diameter of the 18-gauge spinneret (838 μm) used to extrude the filaments. Further statistical data on the diameters of the filaments across 1-m long filaments as well as a 12 m long filament obtained in the wet-spinning manufacturing process can be found in Figure S5 (Supporting Information), as Figures S5a,b (Supporting Information), respectively. Optical microscopy images of the 12 m long filament can be found in Figure S5c (Supporting Information). Since the filament coagulated in free form in the bath, it remained not flattened and rather uniform (see Figure S6, Supporting Information) in contrast to those printed on a substrate in many additive-manufacturing-based methods. To ensure complete reactions and water removal, the filaments were left to dry at 30 °C for 24 h. FT-IR spectra of the filaments immediately after spinning and after 24 h, respectively, displayed a drastic decrease in intensity of thiol groups (≈2570 cm^{-1}) and double bonds from acrylate (≈810 cm^{-1}), signifying that much of the thiol-Michael addition reactions were completed (Figure 1e). Differential scanning calorimetry (DSC) revealed a T_{NI} of 76 °C for the as-spun LCE filament (Figure S7, Supporting Information). Since changes in extrusion and uptake speed resulted in intangible filaments, we varied acrylate-to-thiol molar ratios to optimize the precursor spinning ink to withstand the greatest mechanical deformation without breakage. In turn, we could maximize the freedom to yield more dynamic actuation profiles via mechanical alignment. We found that filaments prepared from an acrylate-to-thiol molar ratio of 1:0.9 demonstrated the largest breaking strains (Figure S8a, Supporting Information). Similarly, when all of the filaments of various molar ratios were drawn to their respective breaking strain (Figure S8b, Supporting

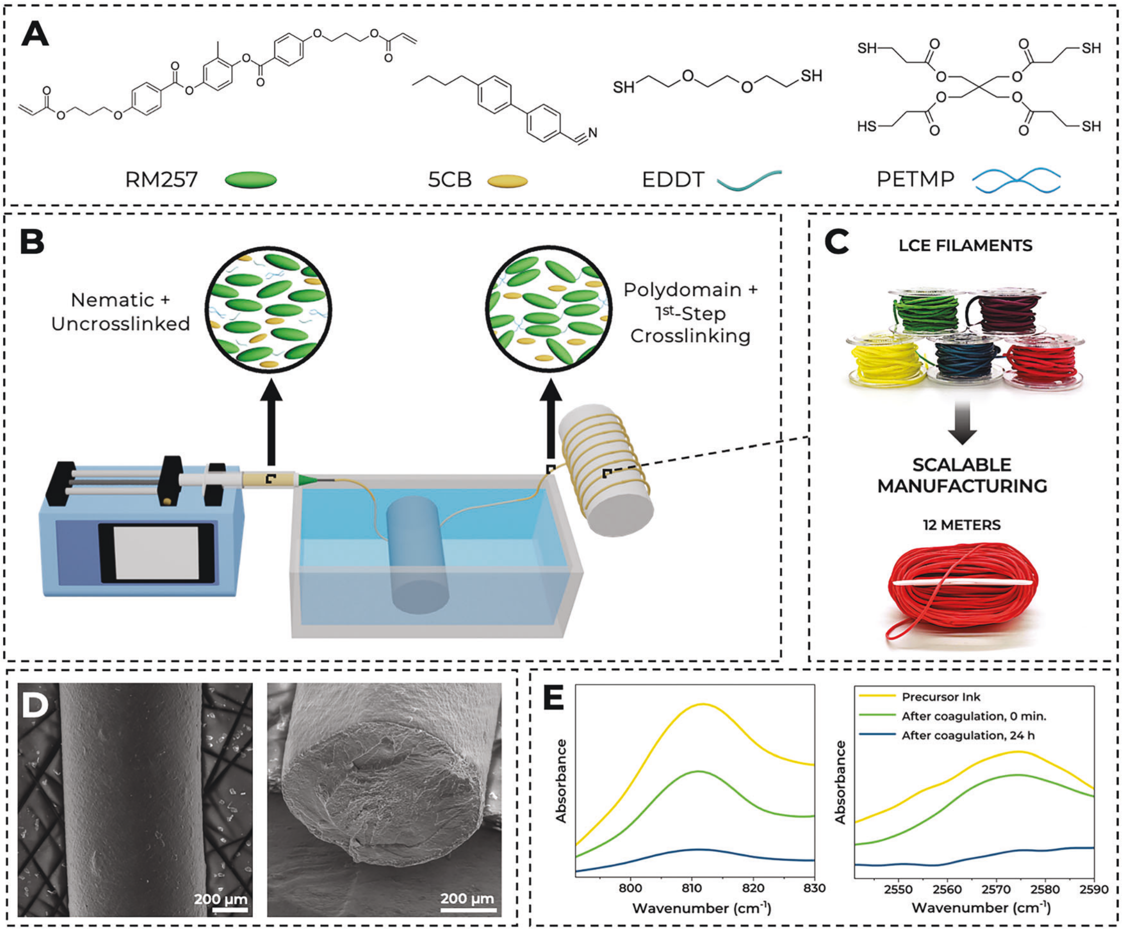

Figure 1. Fabrication of polydomain LCE filaments via the wet-spinning process. a) Schematic illustrations of the chemical structures of the reagents used in the precursor spinning ink. b) Schematic illustrations of the wet spinning process. c) Photos of the wet-spun LCE filaments dyed in different colors up to 12 m long (see Experimental Section for details on dyeing). d) Scanning electron microscopy (SEM) images of a polydomain LCE filament in longitudinal and cross-sectional views. e) Fourier-transform infrared (FT-IR) spectra of the acrylate peak (C=C vibrations, ≈810 cm^{-1}, left) and thiol peak (S-H vibrations, ≈2570 cm^{-1}, right) of the precursor ink before and after coagulation.

Information), the 1:0.9 acrylate-to-thiol ratio yielded the highest actuation strain upon heating (up to 45% when drawn and crosslinked at 133% of the original length).

The developed wet-spinning process offers several advantages: 1) It can produce cylindrical, polydomain LCE filaments, in which we were able to obtain 12-meter-long polydomain filament (see Movie S1, Supporting Information for automated fabrication). Air trapped within the syringe of the spinning ink could lead to variations in filament diameter, or breakage of the coagulating filament that would prevent continuous manufacturing. Therefore, careful degassing or centrifugation of the ink after being loaded inside the syringe before extrusion is essential, especially when spinning with larger syringe volumes. 2) Diverse alignment profiles can be post-programmed via mechanical deformation; monodomain filaments can be obtained at ≈1.3 times the original as-spun length. 3) Nanofillers, such as cellulose nanocrystals, carbon nanotubes, and carbon black, can be coagulated into the meter-long LCE filaments, respectively, for additional functionalities (see Figure S9, Supporting Information).

2.2. Mechanical Alignment of Polydomain LCE Filaments

Mesogen orientation within the filament was characterized by small-angle X-ray diffraction (SAXS). The as-spun LCE filament showed a uniform diffraction ring, suggesting random orientation of the aligned mesogens (Figure S10a, Supporting Information). Efforts in decreasing needle size to yield a polydomain filament resulted in a monodomain filament. When spinning filaments with a 20G needle (≈603 µm), SAXS characterization displayed a monodomain alignment in contrast to the polydomain alignment in using an 18G needle (Figure S10b, Supporting Information) due to the greater shear force generated from a thinner extrusion needle (shear stress is inversely proportional to nozzle diameter). Attempts to apply the automated alignment processes to filaments made with the 20G needle often led to breakage of the filament due to the greater shear forces applied to the thinner filament and overall, unreliable mechanical induction of alignments. For this reason, we moved forward with using an 18G needle for the remainder of the experiments. We recognize that smaller diameters for LCE filaments could

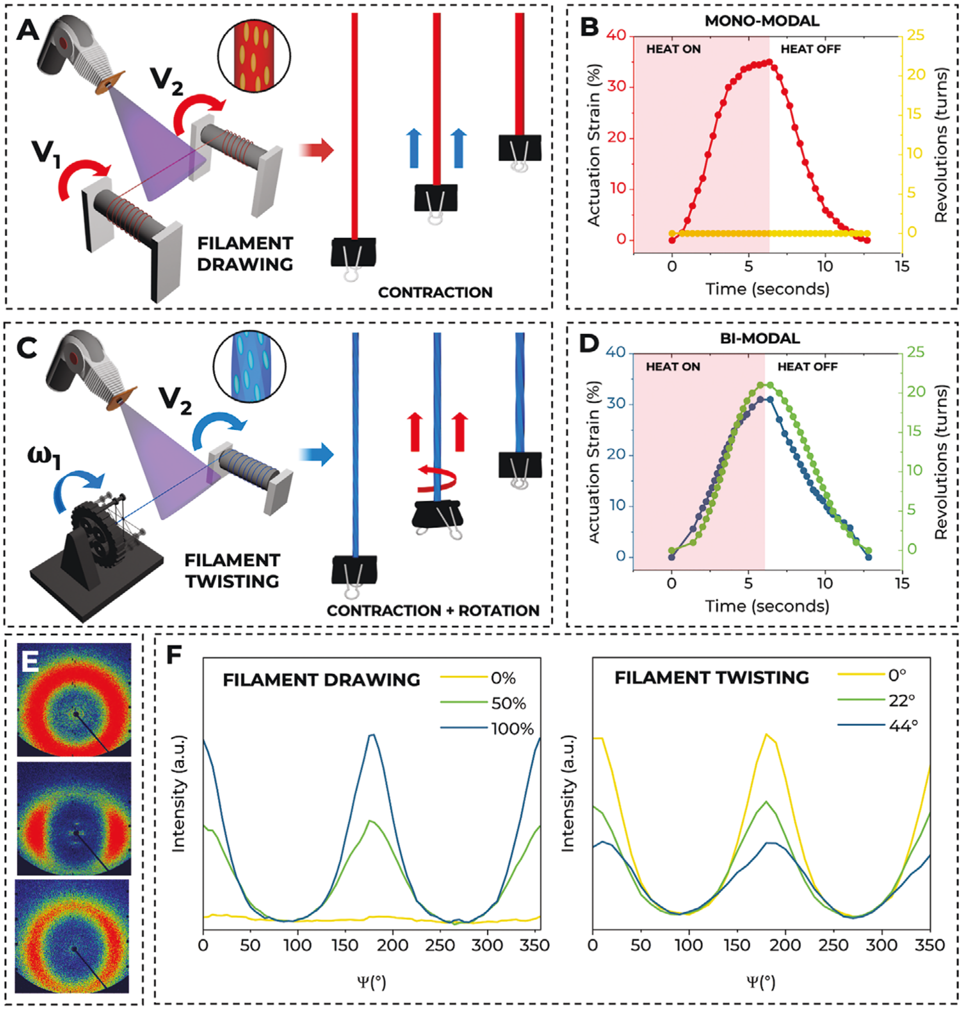

Figure 2. Mono-modal and bi-modal LCE filaments. a) Schematic illustration of the alignment process to fabricate mono-modal filaments and single actuation behavior, contraction. b) Actuation strain and actuation rotations of a mono-modal filament heated at ≈100 °C. c) Schematic illustration of the alignment process for fabrication of bi-modal filaments and their dual actuation behaviors: contraction and rotation. d) Actuation strain and actuation rotations of a bi-modal filament heated at ≈100 °C. e) Small-angle x-ray diffraction patterns of polydomain (*top*), mono-modal (*middle*), and bi-modal (*bottom*) LCE filaments, respectively. f) Azimuthal plots of the LCE filament drawing (*left*) and twisting (*right*).

offer a greater hierarchy in textiles,[1] as well as faster actuation speeds[9] and higher actuation stresses, which are desired for applications such as soft robotics.[4,7] Inclusion of nanofillers within the spinning formulations could improve the mechanical properties of the filaments[4,7] and allow for automated production of smaller diameter filaments. The monodomain filament produced at lower gauges can also be mechanically aligned,[33] which will be of interest in further studies. Further, surfactants could be added to the coagulation bath to align the LC mesogens at the interface, leading to diverse actuation profiles.[26]

With a breaking strain of ≈133% for the polydomain filaments (Figure S8a, Supporting Information), we explored two different alignment mechanisms inspired by conventional textile manufacturing processes to yield mono- (contraction) or bi-modal (contraction and twisting) actuation behaviors (**Figure 2**). To visually distinguish the two alignment mechanisms, the mono-modal and bi-modal filaments are colored red and blue, respectively.

To manufacture mono-modal filaments, a drawing process was conducted on the as-spun filaments using two rollers at varying speeds (Figure 2a, left) (see Experimental Section) to induce a mechanical strain, maximal at 100% of its original length with the stresses of processing, followed by UV cross-linking at filament collection to lock the deformed state. The drawing of the mesogens along the length of the filament yields a contraction upon thermal stimulus (Figure 2a, right). Detailed microscopic and alignment characterizations from 0 to 100% strain are presented in Figure S11 (Supporting Information). The polydomain filament exhibited a decrease in diameter and an increase in alignment evidenced by the two distinct arcs in the SAXS pattern as the drawing percentage increased (Figure S11f, Supporting Information). The mono-modal filaments showed a maximal actuation strain of 35% (Figure 2b; and Movie S2, Supporting Information).

To manufacture bi-modal filaments, a twisting and drawing process (Figure 2c, left) was applied to the as-spun filaments using two rollers, one of which had a twisting element to integrate a bias angle of 44° (see Experimental Section) on a filament pre-drawn at a mechanical strain of 100% of its original length. The added twist was followed by UV cross-linking at the collection of the filament to lock the twisted aligned state. While drawing the filament aligns the mesogens along the length of the filament (see schematic inset in Figure 2a), applying a twist along the length of the filament applied an angular orientation onto the mesogens similar to that of the bias angle. A mechanical strain of 100% and a bias angle of 44° were found to be the maximal that could be reached while withstanding the mechanical stresses of alignment from the automated machinery. The drawing and twisting of the mesogens along the length of the filament yielded contraction and twisting behaviors upon thermal stimulus (Figure 2c, right). SEM images and SAXS patterns seen in Figure S12 (Supporting Information) showed that as the bias angle increased, the twisted filament decreased in diameter and became increasingly isotropic; this behavior is attributed to an enhanced equatorial reflection caused by twisted mesogens.[29] The twisted orientation of the mesogens culminates into the twisted actuation profile on the macroscale, while the general alignment along the length of the filament creates the contraction. The bi-modal filaments showed a maximal actuation strain of ≈31% and the maximal rotation reached a maximum of 21 revolutions (Figure 2d; and Movie S2, Supporting Information). The decreased actuation strain of the bi-modal filaments compared to the mono-modal filaments results from the increase in filament length as a result of the filament untwisting during actuation.[27] For further in-depth analysis of parameters related to actuation performance, we guide the readers to previous efforts from our group.[28]

In comparison to other twisted LCE filaments reported in the literature,[27–29] the bi-modal filaments prepared here are capable of fewer rotations upon actuation, whereas previous work has reported up to ≈80 rotations when actuated at 130 °C.[27] We believe the decreased rotational performance results from the lower twist densities that were applied to the filaments.[28] Ref. [[27]] achieved twist densities of 219° mm^{-1}, whereas our alignment methods were capable of achieving a twist density of 137° mm^{-1} reliably before breaking due to the stresses in the machinery. We attribute this to the decreased diameter of our filaments in comparison to those reported in the literature (>1 mm),[27–29] in which it has been concluded that greater diameters allow for greater twist densities to be applied, and thus have greater rotational performance upon actuation.[28,29] Despite the lower twist density, our method is capable of scalably creating these actuation profiles in tens of meters of LCE filaments in contrast to the centimeter-long twist fibers fabricated by mold-based methods.[27–29] The demonstrated scalability opens the door for broadening the range of actuation profiles in higher-order LCE structures, which is the focus of this manuscript. The demonstrated wet spinning methodology could be leveraged for manufacturing larger filament diameters with increased nozzle sizes, which are more conducive to maximizing the rotational actuation performances of twisted LCE filaments.

Figure 2e shows the SAXS patterns of the final alignments for mono-modal and bi-modal LCE filaments compared to their polydomain precursor. Corresponding azimuthal plots in Figure 2f depict increased peak intensity in mono-modal alignments with a greater draw, while bi-modal filament alignments show increased peak width due to equatorial reflections from twisted mesogens.[32]

2.3. Fabrication of Mono-Modal and Bi-Modal LCE Yarns

Next, we explored the fabrication of LCE yarns and the relationship between mesogen alignment and yarn architecture to elucidate the impacts on mechanical and actuation behaviors. During yarn fabrication, the two single filaments are twisted together, in the opposite direction from which they are spun. The direction of twist, or arrangement of the filaments overlapping with one another, is denoted as Z- or S-twist, that is left- or right-handed twisting, respectively. While the direction of yarn twist generally has relatively little effect on yarn properties and has more effect on the properties when scaled into a fabric[34] (e.g., anisotropy of fabric, reflectance), here, we specifically spun the S-twisted bi-modal filaments into Z-twisted yarns to negate the effects of intrinsic twist on the mechanical properties of the fabricated yarns and focus our analysis on the twist concentration. The opposing hierarchical twists allow for the twist concentrations to be maintained and not unraveled. Similarly, the mono-modal filaments were Z-twisted for yarn construction to control the directionality of twist across all experiments. Here, we plied each type of filament with itself using a plying machine (**Figure 3**a) to yield mono-modal and bi-modal LCE yarns, respectively, with twist concentrations of 2 to 4 twists per cm (Figure 3b). Below 2 twists per cm, filaments could not maintain their ply structures, often unraveling upon actuation, whereas above 4 twists per cm, the yarns became brittle to sustain the mechanical stresses of the plying machine, thus they would break.

After plying mono-modal filaments together (Figure 3c), the actuation strain decreased with the increase of twist concentration; the highest actuation strain of 30.5% was obtained at 4 twists per cm, ≈4.5% decrease from that of the pristine filament (Movie S4, Supporting Information). The plied bi-modal yarns showed a similar trend (Figure 3d); at 4 twists per cm, the actuation strain decreased to ≈27.9%, ≈3% decrease from that of the pristine filament (Movie S5, Supporting Information). The actuation rotation in the bi-modal yarn was reduced dramatically to 4.5 revolutions, a 78.5% decrease compared with its pristine filament. This large drop could be attributed to the notable number of constrictions from the twists imposed from plying.

As we anticipated, at a lower twist concentration (2 twists per cm), actuation performance was better maintained: ≈34% actuation strain for the mono-modal yarn, and ≈29% actuation strain and 13 rotations for the bi-modal yarn. Interestingly, at a higher twist concentration (4 twists per cm^{-1}), the drop in actuation strain was not as large as expected despite the greater number of constrictions from plying. We speculate that this is because the same type of LCE filaments are plied together, in which the elasticity of LCE allows for synergistic contraction with each other. This is further evidenced when plying an elastic LCE filament with a rigid, non-actuating filament (such as nylon); this combination caused the yarn to buckle in a snapping behavior, instead of contracting elastically (Movie S6, Supporting Information).

Next, we characterized the mechanical performance of the fabricated LCE filaments and yarns. **Figure 4** depicts the tensile

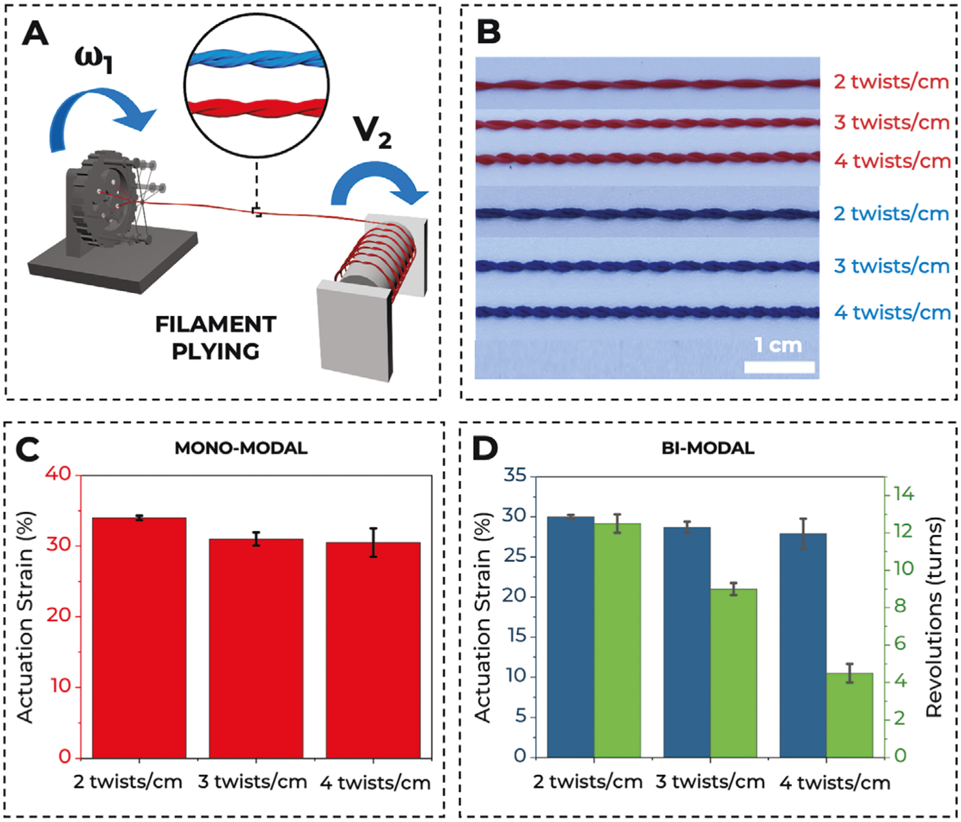

Figure 3. Plied mono-modal and bi-modal LCE filaments. a) Schematic illustration of the plying process for fabrication of mono-modal and bi-modal LCE filaments. b) Digital images of mono-modal and bi-modal LCE yarns with varying twists per cm. c) Actuation strains of mono-modal LCE yarns with varying twists per cm heated at ≈100 °C. d) Actuation strains and actuation rotations of bi-modal LCE yarns with varying twists per cm heated at ≈100 °C.

testing of the filaments (before and after alignment) and of the LCE yarns. Polydomain LCEs are known for soft elasticity;[35] our tensile results agreed well with literature (Figure 4a).[36] After alignment, the breaking strain of the mono-modal and bi-modal filaments decreased to ≈65% and 67%, respectively, whereas the elastic modulus increased from 10 kPa (polydomain) to 50 kPa (mono-modal) and 51 kPa (bi-modal), respectively. The five-fold increase in elastic modulus could be attributed to the alignment of the filament, followed by the cross-linking reactions. It is well-reported that the Young's modulus of LCEs in the aligned direction is Three to four-fold higher than that in the perpendicular direction.[14,35–39] The modulus of polydomain LCE is softer than both of them.[35–39] The bi-modal filaments showed a slightly higher degree of brittleness compared to the mono-modal filaments, which could be attributed to the added twist deformation along the length of the filament.[32] Despite the anticipated drop in actuation characteristics upon plying the aligned LCE filaments together, the mechanical

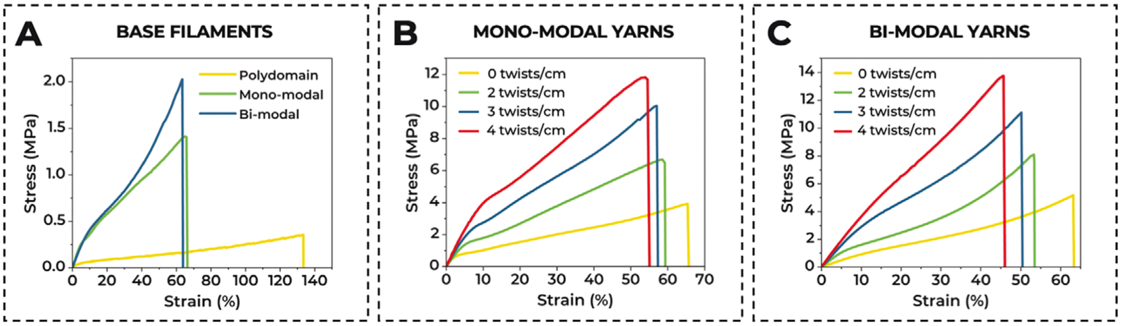

Figure 4. Tensile stress-strain curves of various LCE filaments (acrylate-to-thiol ratio of 1:0.9) and the resulting yarns. a) Polydomain, mono-modal (drawn at 100% of original length), and bi-modal LCE filaments (drawn at 100% of the original length, twisted to a bias angle of 44°). b,c) LCE yarns constructed from mono-modal b) and bi-modal c) filaments with varying plies per cm.

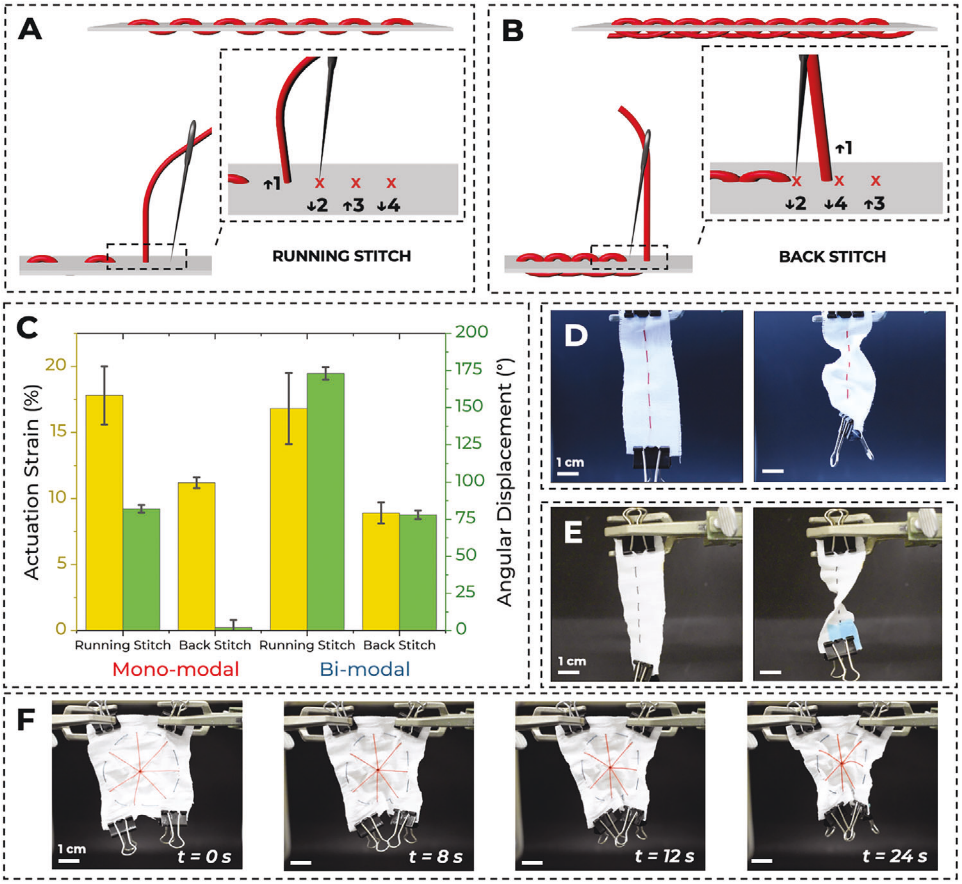

Figure 5. Actuation behaviors of fabrics embroidered with mono-modal and bi-modal LCE filaments onto cotton gauze fabrics. Diagram of embroidery using a) running and b) back stitches. c) Comparison of actuation performances for running and back stitch constructions and type of LCE filament used. d,e) Actuation behavior of a d) mono-modal filament embroidered as a running stitch and a e) bi-modal filament embroidered as a running stitch into cotton gauze fabric. f) Fabric with monomodal and bi-modal LCE filaments actuated across time to induce a directionally-controlled puckering effect. All embroidered fabrics were actuated at ≈100 °C.

properties of the LCE yarns drastically improved with twisting. For both the mono-modal and bi-modal plied yarns, the breaking strain at 0 twist/cm (i.e., two filaments bundled side-by-side) was maintained at 65.7% and 63.3% of the original filament, but the breaking stress increased significantly, from 1.40 and 2.03 MPa to 11.69 and 13.75 MPa, respectively (Figure 4b,c). Upon increasing the twist concentration to 4 twists per cm, the breaking stress increased eight-fold (≈12 MPa) for the mono-modal yarns and over six-fold (≈14 MPa) for the bi-modal yarns.

The data on LCE yarn construction suggests an alternative approach to enhance the mechanical properties of LCEs compared to the use of nanofillers.[7–11] Similarly, yarn construction helped mitigate the loss of actuation strain for mechanical integrity, with the filaments losing only ≈3–4.5% of their native actuation strain when constructed into yarns. Further cyclic characterization of the mono-modal and bi-modal yarns plied at 4 twists per cm averaged an actuation stress of ≈0.7–0.75 MPa (Figure S13, Supporting Information). The value is in good agreement with that of the LCE/carbon nanotube (CNT, 2 wt.%) composite filaments reported by our group,[7] further validating this alternative approach.

2.4. Dynamic Textiles from Embroidered LCE Filaments

Embroidery is a technique that stitches one or multiple threads jointly into a textile in a controlled, patterned manner. In comparison to weaving and knitting, which can require costly manufacturing with processing instrumentation, embroidery offers an opportunity for spatial programming to generate desired 2D-to-3D shape changes in “inactive” substrates such as fabrics and films. While knitting and weaving are limited to axial patterning of LCE filaments and fibers (i.e., fibers are locked to placement in warp/weft or courses/wales),[1] embroidery allows for greater spatial exploration for programming, where axial and concentric placements can be created. Elucidating relationships on stitch type and placement is integral for this realization. Armed with the detailed characterization of the mechanical and actuation behaviors of the mono-modal and bi-modal LCE filaments, we surveyed the effects of common embroidery stitches on the actuation profile and performance of the system. **Figure** 5a depicts the actuation performance of running and back stitches using mono-modal and bi-modal filaments in a cotton gauze fabric. We note that we focus on exploring actuation behaviors from embroidered LCE filaments. This is because LCE yarns, despite showing higher elastic modulus and breaking strains in comparison with their filaments, experienced constrictions from both plying and fabric they were embroidered onto, thus, limiting the achievable maximal actuation strains and rotation performances. Further, the diameter of the yarns is twice of the filament and the mesh size in the cotton gauze used here. Thus, stitching the yarns would require expanding the native meshes in the gauze, causing distortions that could interfere with the actuation. The cotton fabric was chosen for its woven structure and lightweight characteristics. The temperature for actuation in the embroidered samples was confirmed to be ≈102 °C by IR camera imaging (the heat gun was set to heat at 100 °C, see Figure S14c (Supporting Information) for IR images). Across both the mono-modal and bi-modal filaments, the running stitch performed the best in actuation strain and angular displacement. We speculate that this is due to the nature of the stitch configuration, in which the running stitch has much fewer stitch points than the back stitch into the fabric, allowing for greater freedom during actuation. With the mono-modal filament, 50.8% of its native actuation strain was maintained in the running stitch (Figure 5b; and Movie S7, Supporting Information), while 32% was maintained in the back stitch (Movie S8, Supporting Information). Interestingly, we found that the mono-modal filament underwent an angular displacement of ≈9° in the running stitch as a result of the constrictions of the filament in the fabric. As the filament was actuated, the fabric buckled to match the length of the filament, creating an angular displacement. Conversely, negligible angular displacement was found with the back-stitching of the mono-modal filament. Therefore, the fabric did not buckle as much, and thus, did not rotate.

A similar trend was found with the bi-modal filaments. The bi-modal filament maintained ≈54% (Figure 5c; and Movie S9, Supporting Information) and 28.7% (Movie S10, Supporting Information) of its native actuation strain, respectively. For revolutions, the embroidery of the bi-modal filaments resulted in an angular displacement of the gauze fabrics instead of its native rotational actuation. The embroidered bi-modal filament resulted in angular displacements of 173° and 78° when stitched in running and back stitches, respectively. Similar to the mono-modal filaments, the actuation strain decreased drastically for rotations with the back stitch in comparison to the running stitch. The running stitch ran along the length of the fabric embroidered (i.e., in one direction), whereas the stitches on the top and bottom sides of the fabric directly opposed one another in the back stitch. Therefore, when the top and bottom stitches untwisted during rotation, the opposing directions interfered with each other. Similarly for strain, the increased stitches in a back stitch likely prevented the filament from fully contracting compared to the running stitch, which had fewer constrictions and ran entirely in one direction.

To minimize the airflow noise from the heat gun, we chose the lowest airflow setting for our experiments. We confirmed that the airflow did not interfere with the actuation performance of the samples, but could contribute to speeding up the heating of the filament (< 10 s with heat gun, > 40 s with IR lamp, see Figure S14, Supporting Information). The actuation patterns and performance using a heat gun were similar to those obtained using the IR lamp, which heated samples to ≈98 °C as measured by the IR camera in Figure S14d (Supporting Information), except that the time for the fabric to respond was elongated with the infrared lamp. The inclusion of carbonaceous nanofillers can be used to further amplify Joule heating stimuli to decrease the timespan for actuation using an IR lamp.[4,7]

Cyclic characterization of the running stitch embroidered samples showcased significant fatigue after 4–6 cycles at ≈100 °C (Figure S15, Supporting Information) for the mono-modal and bi-modal filaments, respectively. While the samples do largely return to their original state after an actuation cycle due to the load on the fabric samples (≈2.8 g clip), the performance is impeded by frictional barriers between the fabric and LCE filaments, a promising challenge to be addressed in future work. Similarly, efforts in cycling the backstitched samples resulted in fatigue after 1–2 cycles.

Next, we programmed the deformation of the fabric. For a proof-of-concept, we facilitated puckering behaviors in the gauze fabric using mono-modal and bi-modal filaments with directional control (Figure 5d; and Movie S11, Supporting Information) to showcase how the embroidery of an LCE filament could "activate" a 2D-to-3D transformation in an inactive substrate. While puckering behaviors have been shown in LCE thin films,[14,37,40] here, we embroidered a mono-modal LCE filament in an asterisk-like pattern to induce a puckering behavior on a larger scale. The fabric will pucker in either direction depending on the placement of the thermal stimulus. We then embroidered a bi-modal filament in a circular manner around the asterisk-like pattern to limit the puckering actuation to one direction. The use of the bi-modal filament is critical as the programmed rotation from the filament causes the fabric to buckle in a particular direction.

3. Conclusion

We develop a wet-spinning technique to manufacture polydomain LCE filaments, showcasing potential for scalability and can be post-processed by drawing and twisting to create monodomain filaments capable of traditional actuation (contraction) and more complex actuation (rotation and contraction) profiles. When the filaments are plied together into yarns, the breaking stresses increase by 835% and 682% for the mono-modal and bi-modal filaments, respectively. When plied at 4 twists per cm, the actuation strain of the yarns decreases by 3–4.5% relative to that of the pristine filament. We further explore textile structuring by examining embroidery stitch type to the actuation characteristics of LCE filaments. It is found that the running stitches perform the best at maintaining the native actuation characteristics in the inactive fabric. This is then leveraged to embroider mono-modal and bi-modal filaments in radial and concentric manners, respectively, to induce directionally-controlled puckering behaviors in planar "inactive" cotton gauze. This work showcases how diverse alignments in LCE filaments and programming through textile structuring can be used to tailor material performance and deformation performance. Although we have demonstrated applications of our wet-spun filaments for textile applications, they are not limited to textile integration. We expect the development of the wet spinning methodology, and understanding of the mechanism behind the process, to offer new insights into a broad range of applications, e.g. artificial muscles in soft robotics. These insights on the wet spinning of polydomain LCE filaments and the potential to create composites using this technique show promise in transcending LCEs through the textile hierarchy to engineer textiles for thermoregulation, global shaping in fabrics for dynamic fashion, and tailoring locomotion of soft robotics.

4. Experimental Section

Materials: LC monomers, bis-[4-(6-acryloyloxyhexyloxy)benzoyloxy]−2-methylbenzene (RM257, 98%) and 4-cyano-4′-pentylbiphenyl (5CB, 98%) were purchased from AmBeed. Other materials related to LCE synthesis, dipropylamine (DPA, 99%), 2-hydroxy-2-methylpropiophenone (Darocur 1173), and thiol-based reagents, 2,2′-(ethylenedioxy) diethanethiol (EDDET, 95%) and pentaerythritol tetrakis(3-mercaptopropionate) (PETMP, > 95%) were purchased from Sigma–Aldrich. Dyes for coloring LCE filaments, Disperse Red 1, Disperse Blue 1, and Quinoline Yellow, were purchased from Sigma-Aldrich. Cellulose nanocrystals (5–20 nm wide, 150–200 nm long) were purchased from The University of Maine Process Development Center. Carbon black and multiwall carbon nanotubes (MWCNTs, inner diameter 3–5 nm; outer diameter 8–15 nm; length 10–50 µm) were purchased from Cheaptubes. Cotton gauze fabric (85 g m^{-2}) was purchased from Fleishman Fabrics in Philadelphia, PA. All chemicals were used without further purification. All experiments referring to water used deionized water.

Preparation of the LCE Precursor Spinning Ink: To prepare the LCE precursor ink, RM257 and thiol-based chain extenders were placed in a centrifuge container at an acrylate-to-thiol molar ratio of 1:0.9, with an EDDT-to-PETMP molar ratio of 0.7:0.3. This was then followed by the addition of 40 wt.% 5CB and 2 wt.% Darocur 1173. The ink was then mixed at ambient temperature for 2 min at 2000 rpm.

To color the LCE filaments, 0.002 g of dye for every 2 mL of the LCE precursor spinning ink. For primary colors (red, yellow, blue), individual dyes, Disperse Red 1, Disperse Blue 1, or Quinoline Yellow, were used respectively. For secondary colors (e.g., green, purple), 50/50 w/w mixtures of dyes were used.

Formulation of the Coagulation Bath: The approximated solubility of DPA in deionized water was 0.035 g of DPA per g of water. Both DPA and water were combined and stirred for 5 min. at room temperature. The solution was allowed to settle for 30 min to allow any excess DPA to phase separate from water. The excess top layer (phase-separated DPA) was then decanted.

Wet Spinning of the LCE Filaments: The LCE-precursor ink was transferred into a Luer-Lock syringe and degassed for 30 s at 2200 rpm to remove air bubbles in the formulation. A blunt-tipped 18G needle (ID = 838 µm) needle was locked onto the syringe and the syringe was loaded into the coagulation bath. The holder for the coagulation bath (Figure S3, Supporting Information) was 3D-printed using the Ultimaker 3 Extended with thermoplastic polyurethane material. The speed of extrusion was controlled by a syringe pump (Harvard Apparatus 11 Elite) at 100 µL min^{-1}. The spinning LCE filament was carefully guided under the horizontallyplaced rod in the bath to the winding roller outside the coagulation bath for continuous collection at 5 rpm until all spinning ink was exhausted.

Relationships between the nozzle diameter and shear stress can be derived from the following formula:

$$Shear\ stress\ \tau = \frac{Shear\ Force}{Nozzle\ Area} = \frac{Shear\ Force}{\pi * \left(\frac{d}{2}\right)^2} \tag{1}$$

Drawing of LCEs for Mono-Modal Filaments: To facilitate the addition of 100% strain for the production of aligned LCE filaments, the following quantitative analysis was used:

Using the definition of strain for a filament:

$$Strain\ Imposed\ \ (\%) = \varepsilon = \frac{l_{FINAL} - l_{INITIAL}}{l_{INITIAL}} \tag{2}$$

where variable l represents the length of the LCE filament, the formula can be substituted for include the angular velocities V of the rotation mandrels. To convert from linear to rotational mathematics, the following formula was used:

$$l = r\theta \tag{3}$$

where r represents the radius of the mandrels and θ represents the angular displacement of the filament as it collects onto the mandrel. If the angular velocity of the mandrel was to be defined:

$$V = \frac{\theta}{t} \tag{4}$$

where t represents the total time the mandrel rotates, then it could be substituted to reevaluate Equation S1 (Supporting Information) as:

$$Strain\ Imposed\ \ (\%) = \varepsilon = \frac{V_2 - V_1}{V_1} \tag{5}$$

to represent the angular velocities of the two mandrels. Here, it was assumed that both mandrels had the same radius r and rotated for the same amount of time t. This allows to simply double the angular velocity of one rotating mandrel relative to the other to impose a strain of 100% with respect to the original length of the filament. This filament was then cross-linked with a 365 nm UV light provided by Thorlabs at an output power of 100 mW cm^{-2} at the collecting mandrel to lock this strain/alignment for mono-modal filaments.

Twisting of LCE for Bi-Modal Filaments: To manufacture the LCE bi-modal filaments, the drawing step was first conducted with polydomain LCE filaments described in the previous section, but the cross-linking step was not conducted. This results in a pre-tensioned LCE filament strained at 100% of its original length. With the tensioned LCE filament on a plastic bobbin, the bobbin was loaded onto a plying machine ("ENDLESS", PL4 series by Ropewalk) featuring a rotating plate and collecting mandrel. Here, the twisting process occurred in a step-wise manner in which a bias angle was applied to a particular length of tensioned filament, cross-linked, and then wound to reveal a new length of filament to apply the bias angle to. A twist density τ was applied to length l, given by:

$$\tau = \frac{\Delta\theta}{l} \tag{6}$$

where $\Delta\theta$ represents the torsional angle applied to the LCE filament. This twist density can then be used to tabulate bias angle α using the formula:

$$\alpha = \tan^{-1}(r\tau) \tag{7}$$

where r represents the radius of the drawn filament. In this case, it was found that bias angle of 44° was the largest, reliable bias angle that could be achieved on the plying machine. This filament was then cross-linked with a 365 nm UV light provided by Thorlabs at an output power of 100 mW cm^{-2} at the collecting mandrel to lock the bias angle and strain alignment for bi-modal filaments.

Filament Plying for Yarn Assembly: For yarn assembly, a plying machine ("ENDLESS", PL4 series by Ropewalk) was assembled with plastic sewing bobbins. To ply the yarns, mono-modal or bi-modal LCE filaments were individually wound onto the sewing bobbins using a bobbin winder on a sewing machine (LX3817, Brother Sewing Machine) and loaded onto the plying machine. To control the twists along the length of the assembled yarn, the angular speed of the feeding plate and the linear speed of the take-up spool were precisely controlled to instill a desired twist insertion to each yarn actuator fabricated. The twist insertion in the unit of ply per centimeter can be calculated by the following equation:

$$Twist\ insertion\ \left(\frac{ply}{cm}\right) = \frac{\omega_{feeding}}{v_{take-up\ spool}} = \frac{\omega_{feeding}\ (rpm)}{\omega_{take-up\ spool} * 2\pi r_{take-up\ spool}} \tag{8}$$

It should be noted that all twists inserted into the yarn were loaded onto the yarn and not the individual filaments themselves. Similarly, all filaments were able to sustain yarn twists due to the homogenous addition of twists along the length of the yarns. The filaments were twisted counterclockwise to create a Z-twisted yarn. For actuation experiments, additional fixtures (scotch tape, glue) were added to all yarns at both ends to maintain twist insertion.

Filament and Yarn Actuation: To actuate the filaments and yarns generated in this work, a heat gun from Maxwel Manufacturing was used for fast and localized heating. The heat gun was set ≈10–15 cm away from the LCE samples and set at 100 °C in the lowest airflow mode for actuation experiments. Metallic clips were used to control the sample and weighed 2.8 g. For native filament and yarn experiments, a 4 cm length of the sample was actuated, and for embroidery experiments, ≈1 g of LCE filament was used to embroider on a 7 cm by 2 cm cotton gauze fabric sample for actuation experiments.

Characterizations: SEM images were obtained from FEI Quanta 600 Environmental Scanning Electron Microscopy at 10 kV electron beam under 0.50 Torr vacuum pressure. Optical microscopy characterization for actuation strain of different acrylate-to-thiol molar ratios was conducted on the ZEISS Axio Imager 2 Pol with a Linkam temperature stage LTS 420 using 1-mm-long filaments. FT-IR characterization was conducted using a JASCO FT/IR-6800 spectrometer. DSC characterization was conducted using the Q2000 DSC from TA Instruments.

Tensile testing for all generated LCE filaments and yarns was performed on an Instron 5564 model, and a tensile load cell with capability of 10 N was used. All samples had the same initial length before testing (5 cm) and were pulled till breakage. The speed of the moving load cell was fixed at 20 mm min^{-1}. The stress–strain curve was calculated from the force–displacement curve obtained, the diameters of the generated filaments and yarns, and the initial length of the filaments. Actuation stress testing was conducted on an Instron 4206 Universal Testing Machine. The LCE yarns were heat-cycled eight times at ≈100 °C for ≈10 s (≈10 s on/heated, 10 s off/cooling). Approximately 10 s was the timeframe for the filament sample to reach ≈100 °C as confirmed by the thermal camera.

The x-ray diffraction patterns were collected with a Xeuss 2.0 Dual Source Environmental X-ray Scattering System using a Cu source (1.54 Å wavelength) at a 50 kV voltage and 0.6 mA current. A two-slit configuration was used, with respective dimensions of 0.7-by-0.7 mm and 0.4-by-0.4 mm. The sample chamber was held under a vacuum environment at 20 °C and patterns were taken at a sample-to-detector distance of 16 mm with a 120 s exposure time. All data analysis and corresponding transformations (azimuthal integrations and azimuthal profiles) were done in the Foxtrot analysis software.

Supporting Information

Supporting Information is available from the Wiley Online Library or from the author.

Acknowledgements

This research was supported by the National Science Foundation (NSF) Future Eco Manufacturing Research Grant (FMRG, # CMMI 2037097, to S.Y.) and NSF Graduate Research Fellowships Program (GRFP) (grant #, DGE-2236662, to A.P.M.). The authors acknowledge the use of SEM instruments and the Dual Source and Environmental X-ray Scattering facility supported by the NSF Materials Research Science and Engineering Center (grant #, DMR-2309043) at the University of Pennsylvania. The purchase of the Dual Source and Environmental X-ray Scattering facility was made possible by a NSF Major Research Instrumentation (MRI) grant (#17-25969), an Army Research Office (ARO) Defense University Research Instrumentation Program (DURIP) grant (W911NF-17-1-0282) and the University of Pennsylvania. The authors also thank Benjamin Ferko and Max S. Win for critical assistance with SAXS data collection. A.P.M. also gratefully acknowledges the support from the National GEM Consortium through the GEM Fellowship.

Conflict of Interest

The authors declare no conflict of interest.

Author Contributions

A.P.M. and S.Y. conceived the research ideas. A.P.M. and A.N. prepared and fabricated the materials. A.P.M. conducted SAXS, FTIR, mechanical, actuation, and morphological characterizations. S.N. conducted DSC characterizations. A.P.M. carried out characterization analysis and designed all textile demonstrations. A.P.M. and S.Y. wrote the manuscript. S.Y. supervised the research. All authors discussed the results and reviewed the manuscript.

Data Availability Statement

The data that support the findings of this study are available in the supplementary material of this article.

Keywords

elastic yarns, embroidery, liquid crystal elastomers, smart textiles, wet spinning

Received: January 13, 2024
Revised: April 2, 2024
Published online: April 11, 2024

[1] D. J. Roach, C. Yuan, X. Kuang, V. C.-F. Li, P. Blake, M. L. Romero, I. Hammel, K. Yu, H. J. Qi, *ACS Appl. Mater. Interfaces* **2020**, *11*, 19514.
[2] V. Sanchez, C. J. Walsh, R. J. Wood, *Adv. Funct. Mater.* **2021**, *31*, 2008278.
[3] P. E. S. Silva, X. Lin, M. Vaara, M. Mohan, J. Vapaavuori, E. M. Terentjev, *Adv. Mater.* **2023**, *35*, 2210689.
[4] J. Sun, W. Liao, Z. Yang, *Adv. Mater.* **2023**, *35*, 2302706.
[5] J. Lagerwall, *Programmable Mater.* **2023**, *1*, 9.
[6] M. O. Saed, C. P. Ambulo, H. Kim, R. De, V. Raval, K. Searles, D. A. Siddiqui, J. M. O. Cue, M. C. Stefan, M. R. Shankar, T. H. Ware, *Adv. Funct. Mater.* **2019**, *29*, 1806412.
[7] J. Liu, Y. Gao, H. Wang, R. Poling-Skutvik, C. O. Osuji, S. Yang, *Adv. Intell. Syst.* **2020**, *2*, 1900163.
[8] D. Wu, Y. Zhang, H. Yang, A. Wei, Y. Zhang, A. Mensah, R. Yin, P. Lv, Q. Feng, Q. Wei, *Mater. Horiz.* **2023**, *10*, 2587.
[9] I. H. Kim, S. Choi, J. Lee, J. Jung, J. Yeo, J. T. Kim, S. Ryu, S. Ahn, J. Kang, P. Poulin, S. O. Kim, *Nat. Nanotechnol.* **2022**, *17*, 11.
[10] W. Hou, J. Wang, J. Lv, *Adv. Mater.* **2023**, *35*, 2211800.
[11] Y. Yang, W. Zhan, R. Peng, C. He, X. Pang, D. Shi, T. Jiang, Z. Lin, *Adv. Mater.* **2015**, *27*, 6376.
[12] H. E. Fowler, P. Rothemund, C. Keplinger, T. J. White, *Adv. Mater.* **2021**, *33*, 2103806.
[13] Z. S. Davidson, H. Shahsavan, A. Aghakhani, Y. Guo, L. Hines, Y. Xia, S. Yang, M. Sitti, *Sci. Adv.* **2019**, *5*, aay0855.
[14] Y. Wang, A. Dang, Z. Zhang, R. Yin, Y. Gao, L. Feng, S. Yang, *Adv. Mater.* **2020**, *32*, 2004270.
[15] Q. He, Z. Wang, Y. Wang, Z. Wang, C. Li, R. Annapooranan, J. Zeng, R. Chen, S. Cai, *Sci. Rob.* **2021**, *6*, abi9704.
[16] S. Ahn, T. H. Ware, K. M. Lee, V. P. Tondiglia, T. J. White, *Adv. Funct. Mater.* **2016**, *26*, 5819.
[17] S. V. Ahir, A. Tajbakhsh, E. Terentjev, *Adv. Funct. Mater.* **2006**, *16*, 556.
[18] W. Lehmann, H. Skupin, C. Tolksdorf, E. Gebhard, R. Zentel, P. Krüger, M. Lösche, F. Kremer, *Nature* **2001**, *410*, 447.

[19] X. Lin, M. O. Saed, E. M. Terentjev, *Soft Matter* **2021**, *17*, 5436.
[20] X. Dong, X. Zhou, L. Li, X. Cao, J. Xu, S. Dai, Y. Jiang, Q. Li, N. Yuan, J. Ding, *iScience* **2023**, *26*, 106357.
[21] Y. Geng, R. Kizhakidathazhath, J. P. F. Lagerwall, *Nat. Mater.* **2022**, *21*, 1441.
[22] M. Javadzadeh, J. del Barrio, C. Sánchez-Somolinos, *Adv. Mater.* **2023**, *35*, 2209244.
[23] X. Wang, H. Shao, J. Tang, J. Chen, Y. Huang, J. Pan, Y. Zhang, W. Wang, J. Jiang, N. Chen, *Adv. Mater. Technol.* **2023**, *8*, 2300814.
[24] Y. Sawa, K. Urayama, T. Takigawa, A. DeSimone, L. Teresi, *Macromolecules* **2010**, *43*, 4362.
[25] D. S. Kim, Y.-J. Lee, Y. B. Kim, Y. Wang, S. Yang, *Sci. Adv.* **2023**, *9*, 20.
[26] D. S. Kim, Y.-J. Lee, Y. Wang, J. Park, K. I. Winey, S. Yang, *ACS Appl. Mater. Interfaces* **2022**, *14*, 50171.
[27] Y. Wang, J. Sun, W. Liao, Z. Yang, *Adv. Mater.* **2022**, *34*, 2107840.
[28] Y. Zhao, Y. Chi, Y. Hong, Y. Li, S. Yang, J. Yin, *Proc. Natl. Acad. Sci. USA* **2022**, *119*, 22.
[29] Y. Zhao, Y. Hong, Y. Li, F. Qi, H. Qing, H. Su, J. Yin, *Sci. Adv.* **2023**, *9*, 36.
[30] H. A. Pohl, *Text. Res. J.* **1958**, *28*, 473.
[31] Y. Xia, X. Zhang, S. Yang, *Angew. Chem., Int. Ed.* **2018**, *57*, 5665.
[32] N. V. Hien, S. L. Cooper, J. A. Koutsky, *J. Macromol. Sci. B* **1972**, *6*, 343.
[33] Y. B. Kim, S. Yang, D. S. Kim, *Adv. Sci.* **2024**, *11*, 2308350.
[34] A. Alamdar-Yazdi, S. M. Bidoki, *J. Text. Inst.* **2010**, *101*, 739.
[35] J. S. Biggins, M. Warner, K. Bhattacharya, *J. Mech. Phys. Solids* **2012**, *60*, 573.
[36] A. Azoug, V. Vasconcellos, J. Dooling, M. Saed, C. M. Yakacki, T. D. Nguyen, *Polymer* **2016**, *98*, 165.
[37] Y. Xia, A. Honglawan, S. Yang, *Liq. Cryst. Rev.* **2019**, *7*, 30.
[38] Y. Wang, J. Liu, S. Yang, *Appl. Phys. Rev.* **2022**, *9*, 011301.
[39] Y. Cang, J. Liu, M. Ryu, B. Graczykowski, J. Morikawa, S. Yang, G. Fytas, *Nat. Commun.* **2022**, *13*, 5248.
[40] Y. Xia, A. Honglawan, S. Yang, *Liq. Cryst. Rev.* **2019**, *7*, 30.

ADVANCED
FUNCTIONAL
MATERIALS

Supporting Information

for *Adv. Funct. Mater.*, DOI 10.1002/adfm.202400742

Active-Textile Yarns and Embroidery Enabled by Wet-Spun Liquid Crystalline Elastomer Filaments

*Antonio Proctor Martinez, Alicia Ng, So Hee Nah and Shu Yang**

Supporting Information

Active-textile Yarns and Embroidery Enabled by Wet-spun Liquid Crystalline Elastomer Filaments

*Antonio Proctor Martinez, Alicia Ng, So Hee Nah, and Shu Yang**

Department of Materials Science and Engineering, University of Pennsylvania, 3231 Walnut Street, Philadelphia, PA 19104 USA

This PDF file includes:
- Figs. S1-S15
- Captions for Movies S1 to S11

Other Supplementary Materials for this manuscript include the following:
- Movies S1 to S11

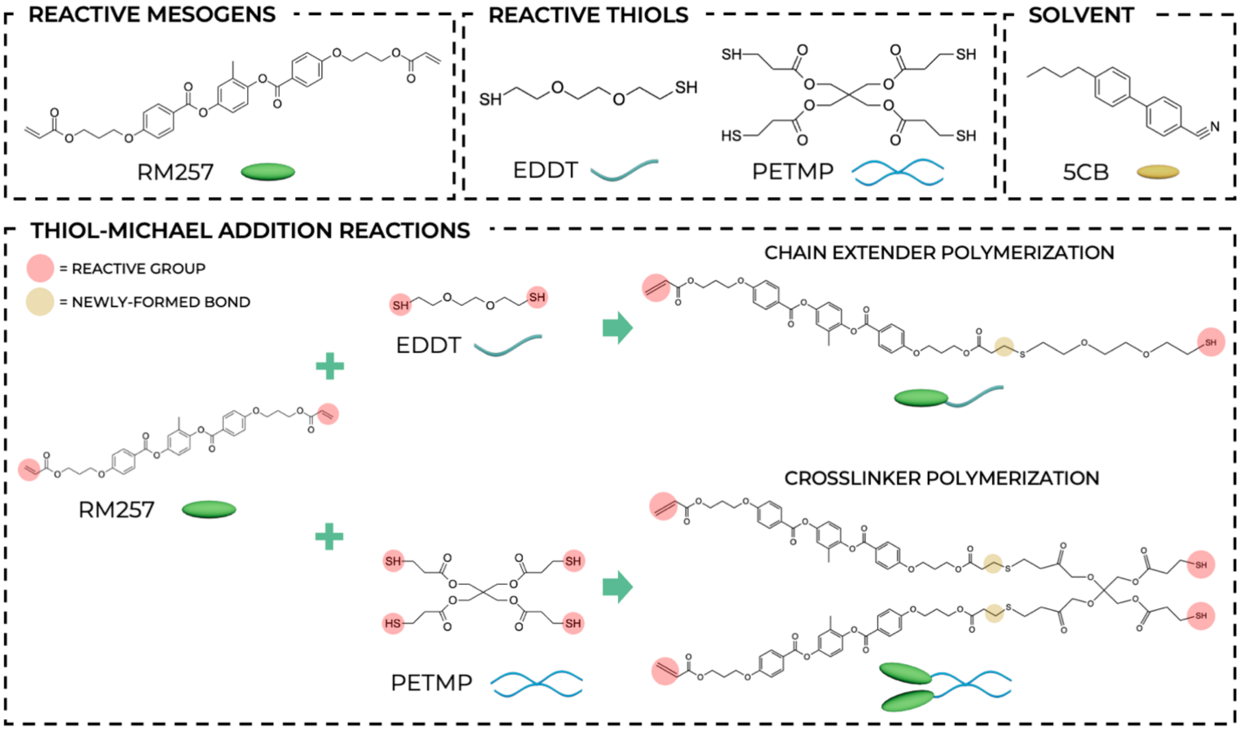

Figure S1. A schematic illustration of the thiol-Michael addition reactions occurring in the wet spinning methodology.

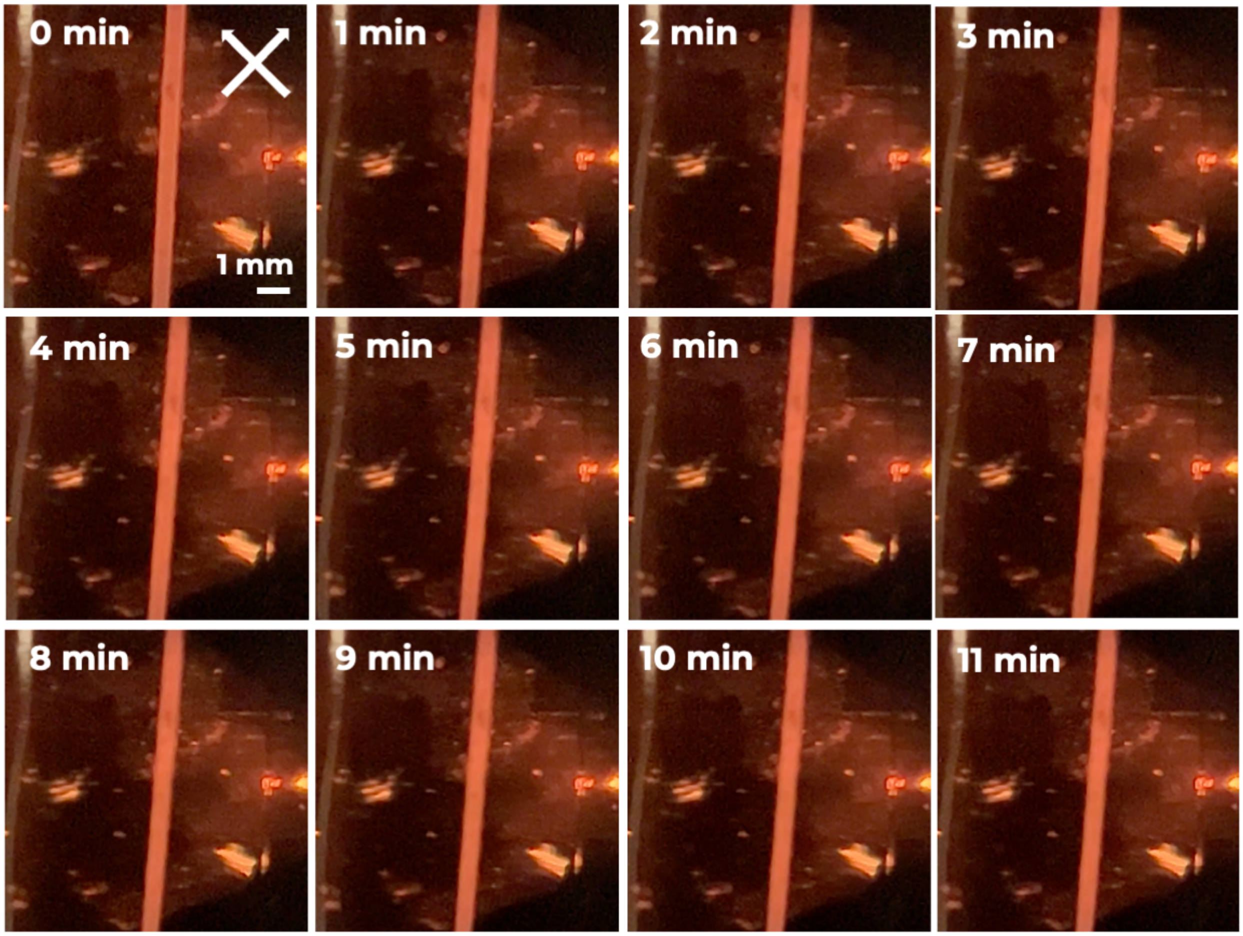

Figure S2. Polarized optical microscopy (POM) images of the LCE precursor spinning ink coagulating into an LCE filament over time. Upon initial extrusion, the formulation is in the nematic state due to the use of 5CB as a solvent and this phase is maintained as it coagulates. Arrows indicate the crossed polarizers.

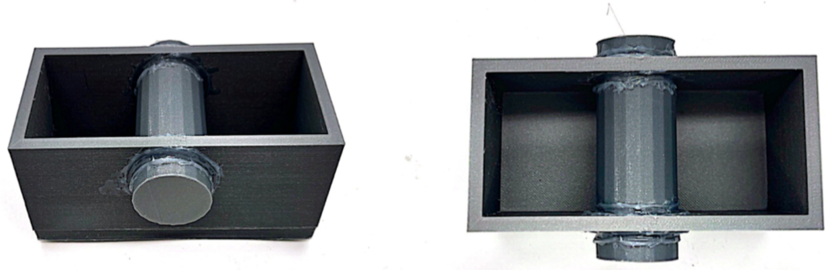

Figure S3. Digital photo of the coagulation bath holder.

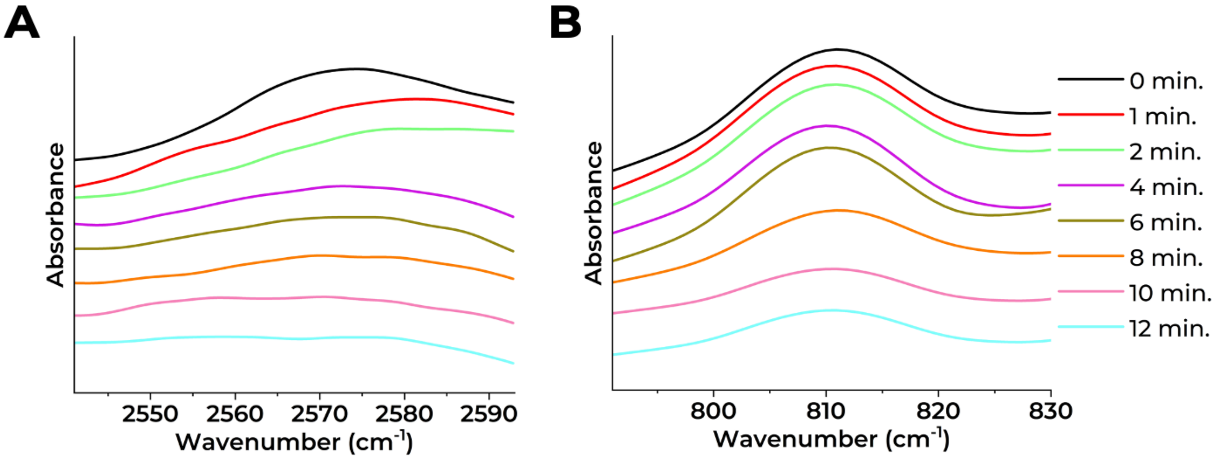

Figure S4. FT-IR spectra of the thiol-Michael-addition reactions in the coagulated filament over time. **(a)** Thiol peak (S - H, ~2570 cm^{-1}) and **(b)** the acrylate peak (C = C, ~810 cm^{-1}). Measurements are taken of a polydomain filament reacting immediately after exposure to the coagulation bath.

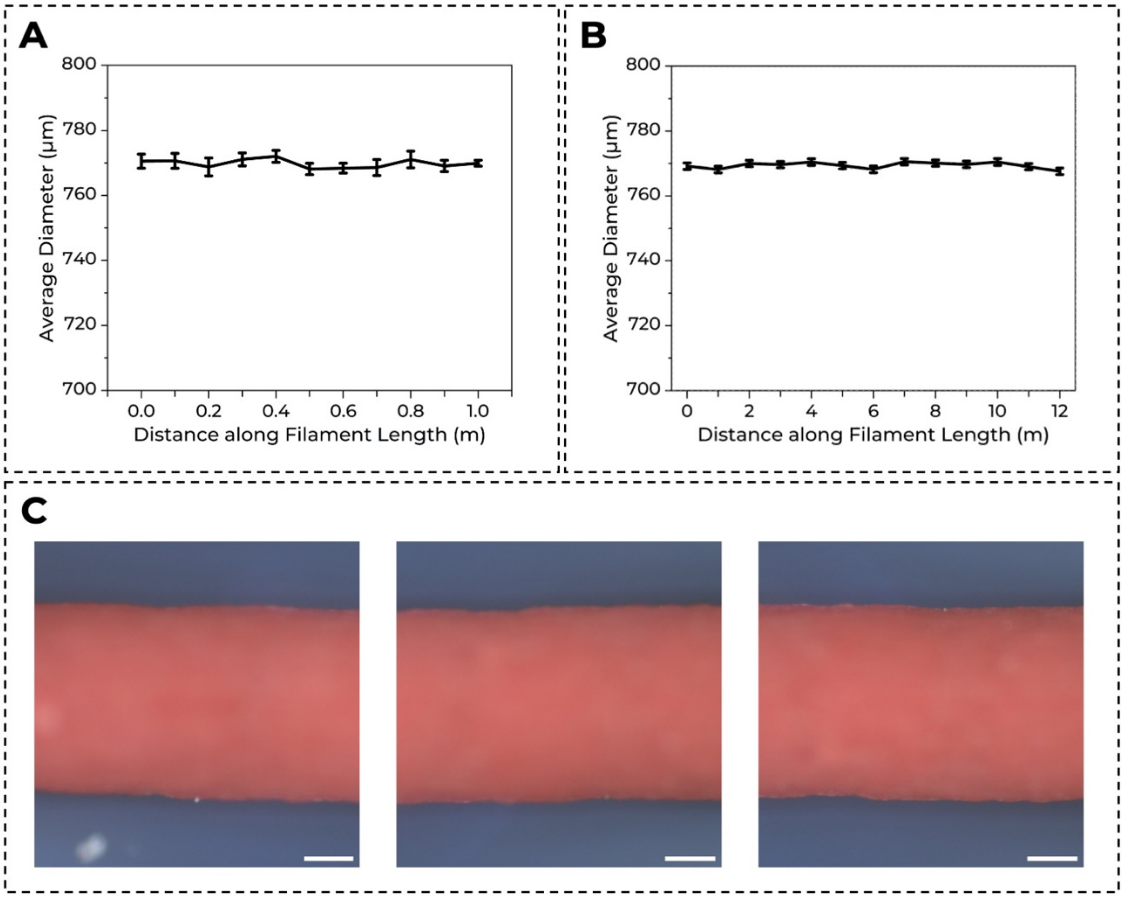

Figure S5. Average diameter measured across the length of wet-spun **(a)** 1-m LCE filaments (5 samples), **(b)** 12-m LCE filament, and **(c)** optical microscopy images of various points along the the 12-m filament (scale bar = 200 µm).

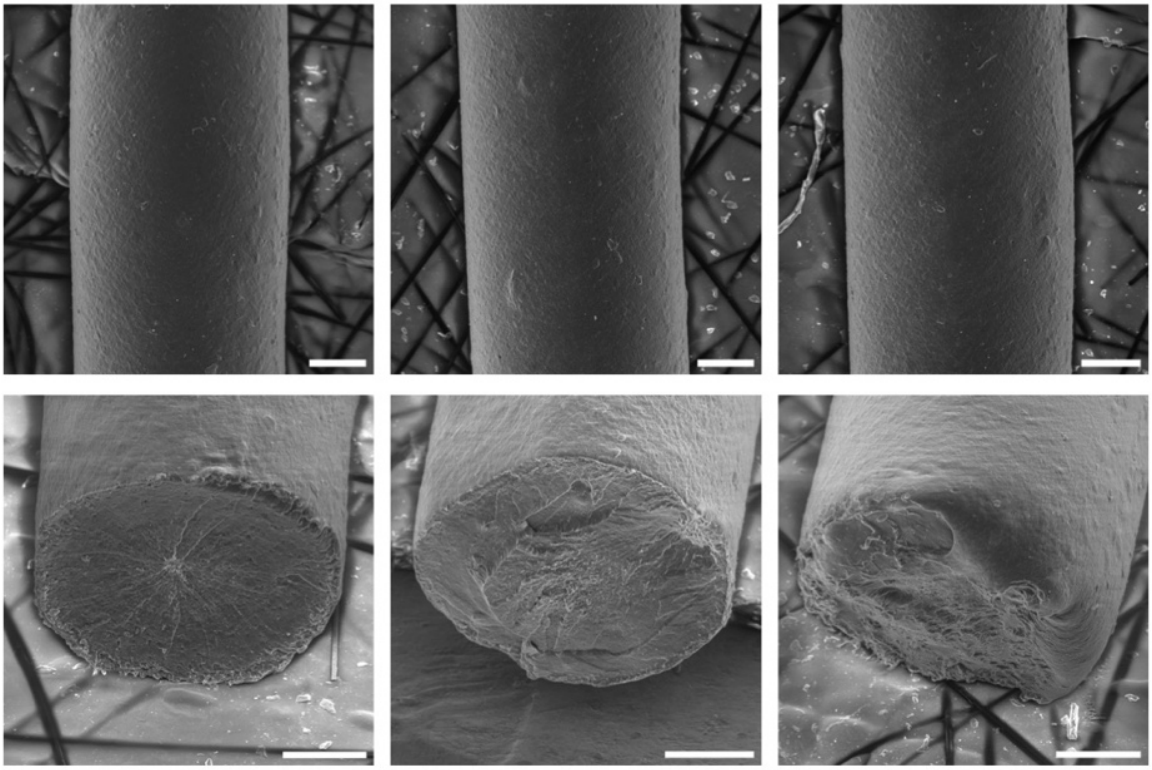

Figure S6. Longitudinal and cross-sectional SEM images of three different polydomain LCE filaments. Scale bar is 200 μm.

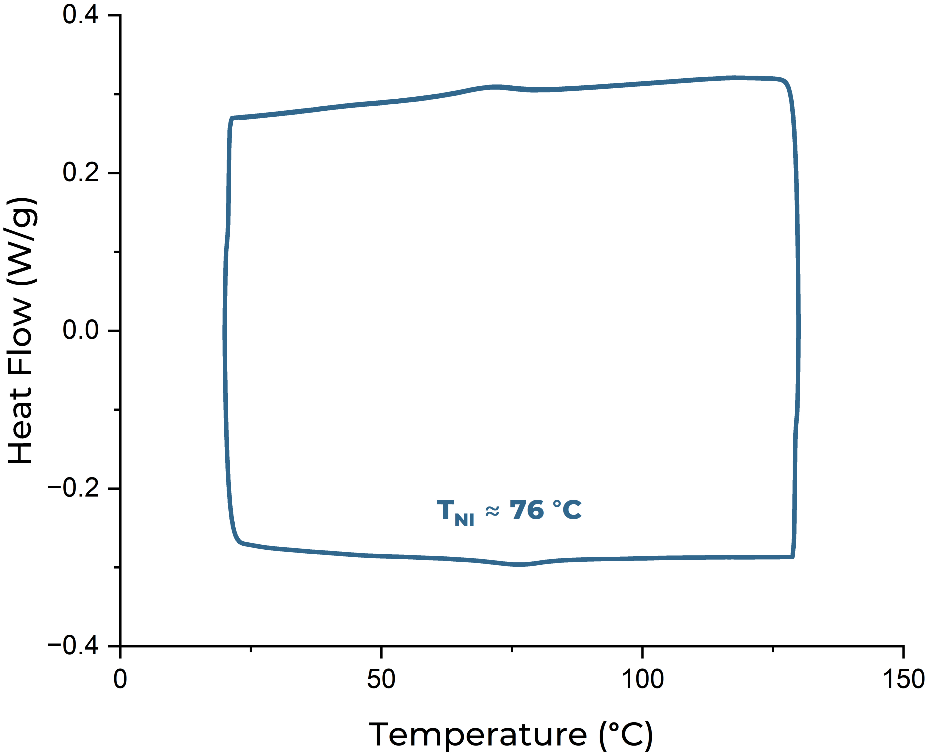

Figure S7. Differential scanning calorimetry (DSC) curves of the heating and cooling cycle of a pristine polydomain LCE filament as-spun from the coagulation bath.

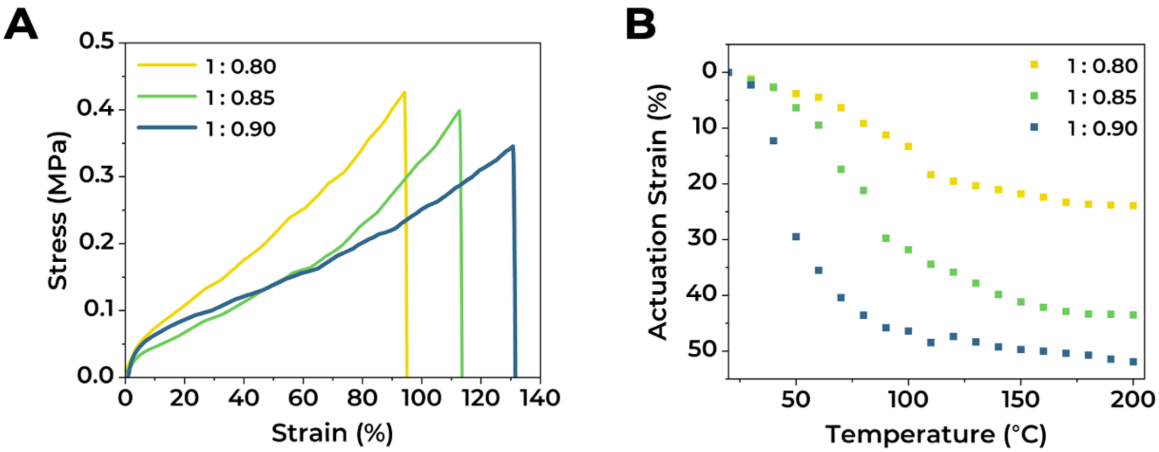

Figure S8. Mechanical and actuation behaviors of the pristine LCE filaments with various acrylate-to-thiol molar ratios. **(a)** Tensile tests along the parallel direction of LC mesogen alignment. **(b)** Actuation strain versus temperatures. All filaments were approximately drawn to their corresponding breaking strains.

Figure S9. Digital photo of meter-long wet-spun LCE composite filaments.

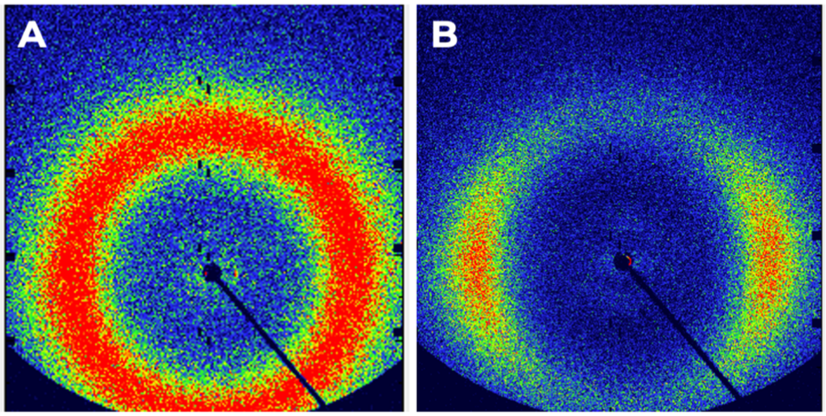

Figure S10. Small-angle x-ray diffraction patterns of an as-spun filament spun from an **(a)** 18G needle (ID ~838 µm) and **(b)** 20G needle (ID ~603 µm).

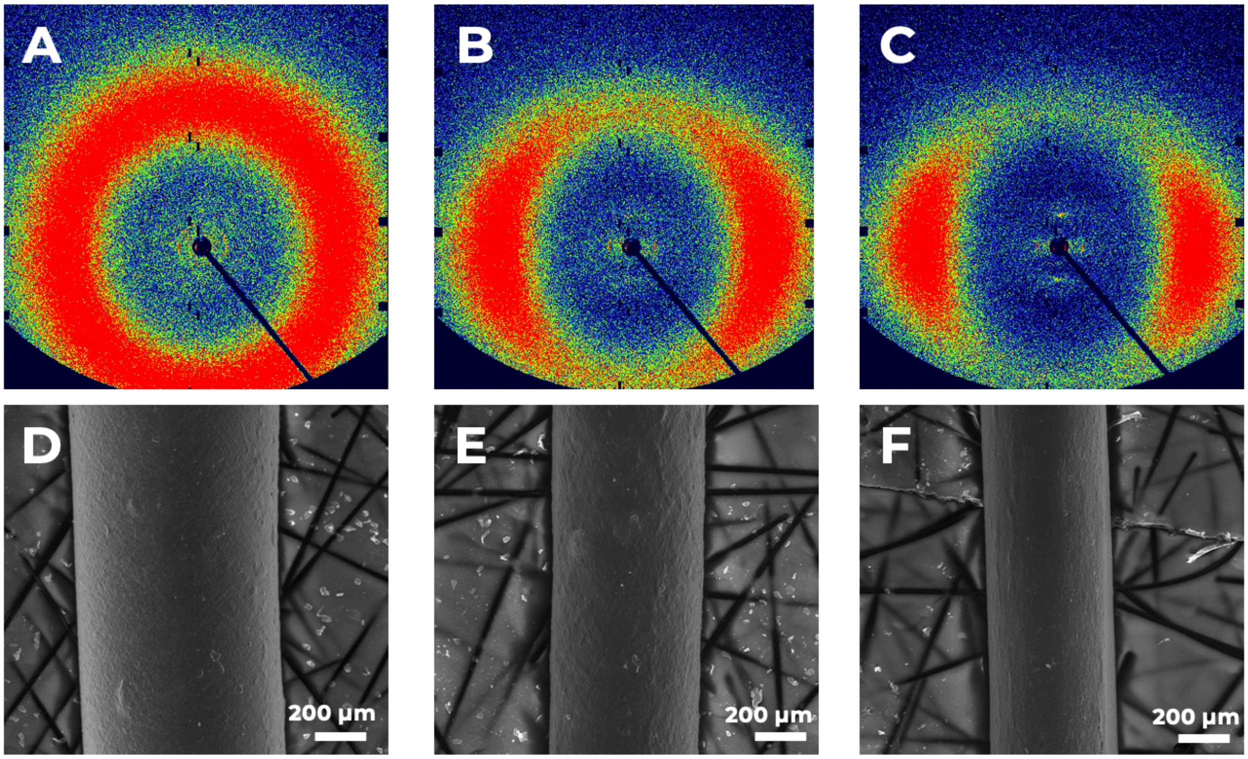

Figure S11. Morphological characterization of drawn pristine LCE filaments. Small-angle x-ray diffraction (SAXS) patterns **(a-c)** and top-view SEM images (**d-f**) of an as-spun polydomain filament drawn at **(a, d)** 0%, **(b, e)** 50%, and **(c, f)** 100% of its original length, respectively.

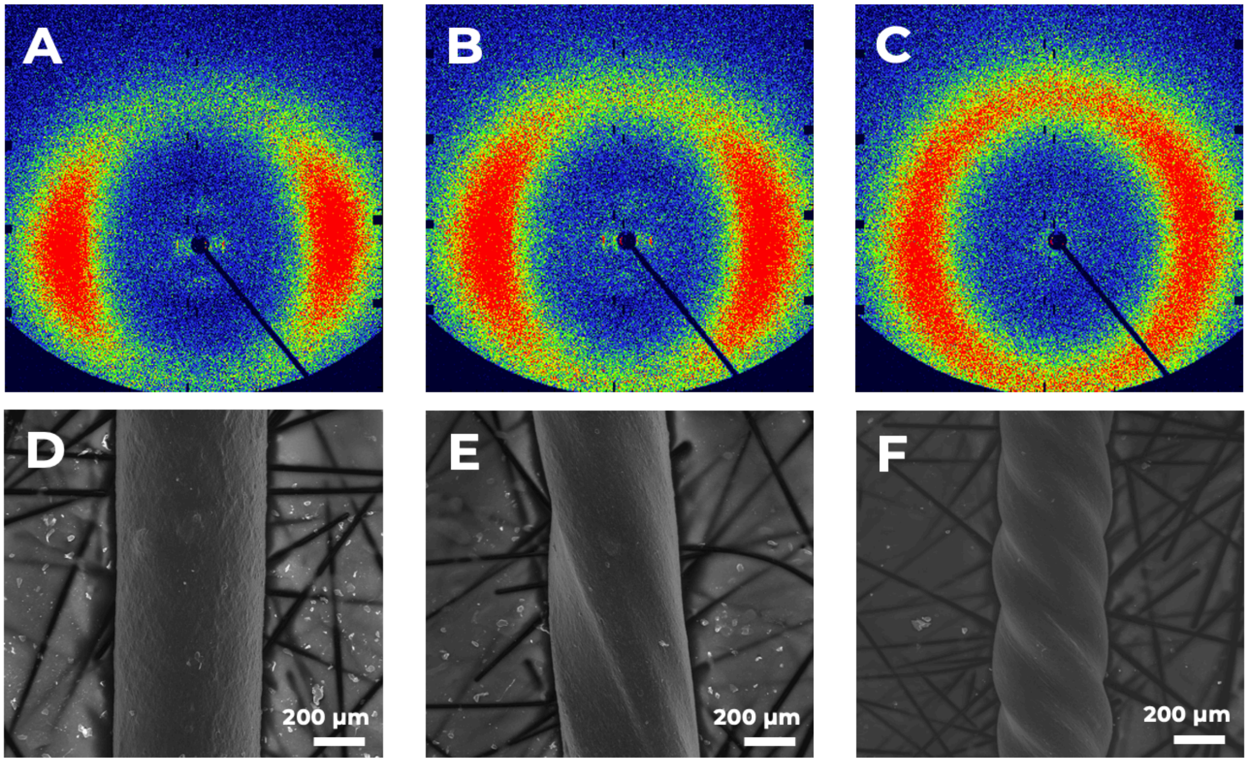

Figure S12. Morphological characterization of drawn and twisted pristine LCE filaments. Small-angle x-ray diffraction (SAXS) patterns **(a-c)** and top-view SEM images (**d-f**) of an as-spun polydomain filament twisted to bias angles of **(a, d)** 0°, **(b, e)** 22°, and **(c, f)** 44° while drawn to 100% of its original length, respectively.

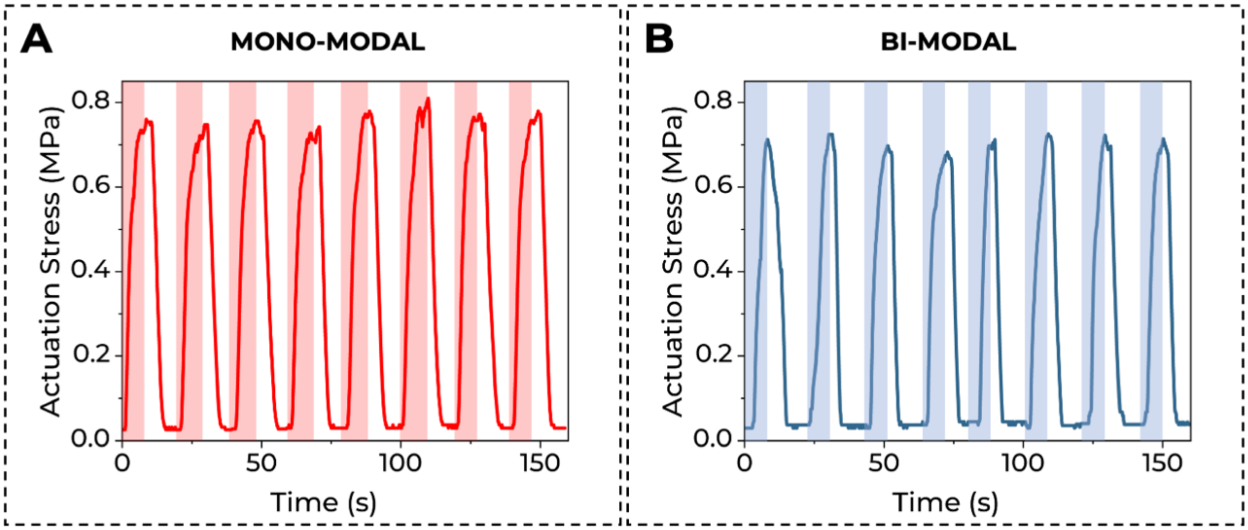

Figure S13. Actuation stress of the plied **(a)** mono-modal and bi-modal **(b)** LCE yarns (twisted at 4 twists/cm) when a heat gun is periodically turned on and off over eight cycles at ~100 °C. The temperature was measured from a thermal camera.

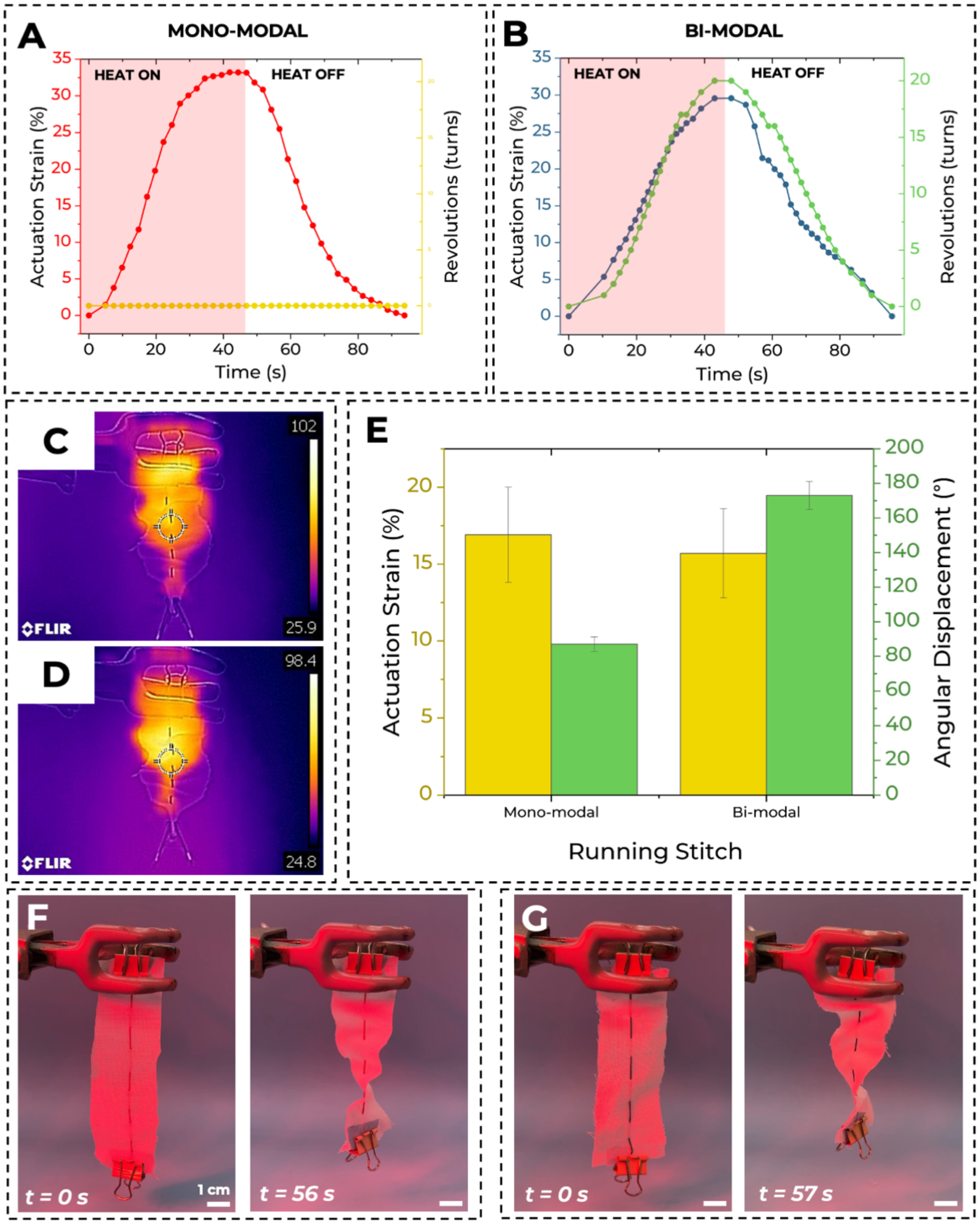

Figure S14. Actuation characterization of the mono-modal and bi-modal filaments, and the respective running stitch embroidered samples upon heating by an infrared (IR) lamp. Actuation performance of **(a)** mono-modal and **(b)** bi-modal filaments heated by an IR lamp (filaments estimated to reach ~98 °C in IR camera). (c-d) Temperature reading from the IR camera on of a running stitch sample used in embroidered samples heated with a **(c)** heat gun at ~100 °C and an **(d)** IR lamp. **(e)** Actuation performance of the running-stitch-embroidered samples upon heating by the IR lamp. **(f-g)** Digital images of the running stitch-embroidered samples actuated with the IR lamp for **(f)** mono-modal and **(g)** bi-modal filaments, respectively.

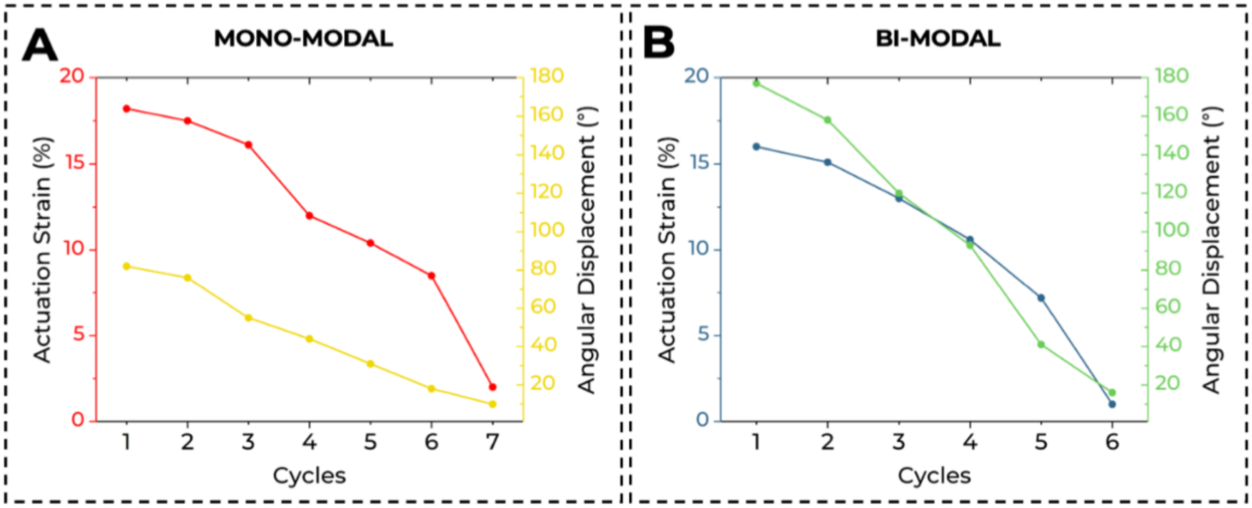

Figure S15. Cyclic actuation of running stitch samples embroidered with **(a)** mono-modal and **(b)** bi-modal filaments, respectively.

Movie captions:

Movie S1. Overview of fiber fabrication process, automated wet spinning methodology, and real-time coagulation of LCE precursor spinning ink.

Movie S2. Actuation of a mono-modal LCE filament under 2.8-gram load. A red mono-modal LCE filament is actuated at ~100 °C.

Movie S3. Actuation of a bi-modal LCE filament under 2.8-gram load. A blue bi-modal LCE filament is actuated at ~100 °C.

Movie S4. Actuation of a mono-modal (4 twists/cm) LCE yarn under 2.8-gram load. A red mono-modal LCE yarn is actuated at ~100 °C.

Movie S5. Actuation of a bi-modal (4 twists/cm) LCE yarn under 2.8-gram load. A blue bi-modal LCE yarn is actuated at ~100 °C.

Movie S6. Actuation of a nylon-mono-modal-LCE-filament yarn plied at 2 twists/cm under a 2.8-gram load. The yarn is actuated at ~100 °C.

Movie S7. Actuation of a mono-modal LCE filament straight-stitched into white cotton gauze fabric. The embroidered fabric is actuated at ~100 °C.

Movie S8. Actuation of a mono-modal LCE filament back-stitched into white cotton gauze fabric. The embroidered fabric is actuated at ~100 °C.

Movie S9. Actuation of a bi-modal LCE filament straight-stitched into white cotton gauze fabric. The embroidered fabric is actuated at ~100 °C.

Movie S10. Actuation of a bi-modal LCE filament back-stitched into white cotton gauze fabric. The embroidered fabric is actuated at ~100 °C.

Movie S11. Actuation of a mono-modal and bi-modal LCE filament embroidered in a circular manner to induce a puckering behavior. The embroidered yarn is actuated at ~100 °C.